

ER-to-lysosome-associated degradation of proteasome-resistant ATZ polymers occurs via receptor-mediated vesicular transport

Ilaria Fregno^{1,2,†}, Elisa Fasana^{1,†}, Timothy J Bergmann^{1,2}, Andrea Raimondi³, Marisa Loi^{1,2}, Tatiana Soldà¹, Carmela Galli¹, Rocco D'Antuono¹, Diego Morone¹, Alberto Danieli⁴, Paolo Paganetti⁵, Eelco van Anken⁴ & Maurizio Molinari^{1,6,*} 

Abstract

Maintenance of cellular proteostasis relies on efficient clearance of defective gene products. For misfolded secretory proteins, this involves dislocation from the endoplasmic reticulum (ER) into the cytosol followed by proteasomal degradation. However, polypeptide aggregation prevents cytosolic dislocation and instead activates ill-defined lysosomal catabolic pathways. Here, we describe an ER-to-lysosome-associated degradation pathway (ERLAD) for proteasome-resistant polymers of alpha1-antitrypsin Z (ATZ). ERLAD involves the ER-chaperone calnexin (CNX) and the engagement of the LC3 lipidation machinery by the ER-resident ER-phagy receptor FAM134B, echoing the initiation of starvation-induced, receptor-mediated ER-phagy. However, in striking contrast to ER-phagy, ATZ polymer delivery from the ER lumen to LAMP1/RAB7-positive endolysosomes for clearance does not require ER capture within autophagosomes. Rather, it relies on vesicular transport where single-membrane, ER-derived, ATZ-containing vesicles release their luminal content within endolysosomes upon membrane:membrane fusion events mediated by the ER-resident SNARE STX17 and the endolysosomal SNARE VAMP8. These results may help explain the lack of benefits of pharmacologic macroautophagy enhancement that has been reported for some luminal aggregopathies.

Keywords endolysosomes; ER-phagy; ER-to-lysosome-associated degradation; LC3 lipidation; proteasome-resistant aggregates

Subject Categories Autophagy & Cell Death; Membrane & Intracellular Transport; Post-translational Modifications, Proteolysis & Proteomics

DOI 10.15252/emboj.201899259 | Received 16 February 2018 | Revised 22 June 2018 | Accepted 30 June 2018 | Published online 3 August 2018

The EMBO Journal (2018) 37: e99259

Introduction

About 40% of the eukaryotic cell's proteome is synthesized in the ER (Uhlen *et al*, 2015). Protein folding is rather inefficient (Schubert *et al*, 2000; Vabulas & Hartl, 2005) and maintenance of cellular proteostasis, i.e., the capacity to produce the proteome in appropriate quality and quantity requires continuous removal from biosynthetic compartments of polypeptides that fail to attain the native structure. Paradoxically, the ER does not contain catabolic devices in its lumen. Misfolded ER clients are dislocated in the cytosol for clearance by the ubiquitin-proteasome system (UPS; Guerriero & Brodsky, 2012; Pisoni & Molinari, 2016). Yet, misfolding may in certain cases cause polypeptide aggregation that impairs dislocation and UPS intervention. The disease-causing polymerogenic E342K (ATZ) variant of alpha1 antitrypsin (AT) (Teckman & Perlmutter, 2000; Kamimoto *et al*, 2006; Kroeger *et al*, 2009), various serpin mutants (Kroeger *et al*, 2009), the E90K mutant of the gonadotropin-releasing hormone receptor (GnRHR; Houck *et al*, 2014), the β subunits of thyrotrophic hormone (Noda & Farquhar, 1992), proalpha1(I) chains of type I collagen (Ishida *et al*, 2009), and the L1341P mutant of dysferlin (Fujita *et al*, 2007) are reported cases of proteasome-resistant misfolded proteins generated in the ER and degraded with the contribution of the lysosomal system. Core components of the macroautophagy machinery required for membrane-tethering of the cytosolic ubiquitin-like LC3 and/or GABARAP proteins (e.g., ATG5, ATG7, or VPS34/BCN1) are involved in lysosomal clearance of these proteasome-resistant polypeptides (Teckman & Perlmutter, 2000; Kamimoto *et al*, 2006; Fujita *et al*, 2007; Ishida *et al*, 2009; Kroeger *et al*, 2009; Gelling *et al*, 2012; Houck *et al*, 2014). Originally, LC3 lipidation was reported to occur at the phagophore membrane, as an early event in biogenesis of double-membrane autophagosomes regulating macroautophagy (Suzuki *et al*, 2007; Mizushima *et al*,

1 Faculty of Biomedical Sciences, Institute for Research in Biomedicine, Università della Svizzera italiana (USI), Bellinzona, Switzerland

2 Department of Biology, Swiss Federal Institute of Technology, Zurich, Switzerland

3 Experimental Imaging Center, San Raffaele Scientific Institute, Ospedale San Raffaele, Milan, Italy

4 Division of Genetics and Cell Biology, San Raffaele Scientific Institute, Ospedale San Raffaele, Milan, Italy

5 Laboratory for Biomedical Neurosciences, Neurocenter of Southern Switzerland, Taverne-Torricella, Switzerland

6 School of Life Sciences, École Polytechnique Fédérale de Lausanne, Lausanne, Switzerland

*Corresponding author. Tel: +41 918200319; E-mail: maurizio.molinari@irb.usi.ch

[†]These authors contributed equally to this work

2011). It has therefore been inferred that macroautophagy regulates clearance of proteasome-resistant aggregates from the ER, as it does for cytosolic aggregates (Lamark & Johansen, 2012; Bento *et al*, 2016; Hurley & Young, 2017; Menzies *et al*, 2017). However, luminal aggregates are shielded by the ER membrane from the macroautophagy machinery that operates in the cell cytosol. Thus, an intervention of macroautophagy in clearance of luminal aggregates would imply their dislocation across the ER membrane, or the capture of ER portions containing them by autophagosomes (Marciniak *et al*, 2016). This latter option is particularly intriguing in view of the recent identification of ER-resident, LC3-binding proteins proposed to selectively label ER subdomains for lysosomal clearance via processes collectively defined as ER-phagy (Khaminets *et al*, 2015; Fumagalli *et al*, 2016; Grumati *et al*, 2017; Fregno & Molinari, 2018; Loi *et al*, 2018; Smith *et al*, 2018). Conventional macroautophagy inducers such as rapamycin and starvation enhance clearance of cytosolic inclusions (Lamark & Johansen, 2012; Bento *et al*, 2016; Hurley & Young, 2017; Menzies *et al*, 2017) and of some proteasome-resistant, large polypeptides misfolding in the ER lumen such as pro α 1(I) chains of type I collagen (Ishida *et al*, 2009) and mutant dysferlin (Fujita *et al*, 2007). For ATZ and other serpin polymers and for the E90K GnRHR, however, lysosomal clearance in cellular and animal disease models is not affected, or it is actually impaired, on conventional macroautophagy activation upon mTOR inhibition (Teckman *et al*, 2002; Kroeger *et al*, 2009; Hidvegi *et al*, 2010; Houck *et al*, 2014). Thus, it can be speculated that macroautophagic (rapamycin-responsive) and non-macroautophagic (rapamycin-unresponsive) catabolic pathways operate in mammalian cells to back-up the UPS for clearance of compartmentalized aggregates. In such a scenario, the LC3 lipidation machinery that intervenes in clearance of rapamycin-insensitive substrates could do so in a non-canonical fashion (Bestebroer *et al*, 2013; Kistakis & Tooze, 2016). To explore this notion, we monitored the fate of proteasome-resistant ATZ polymers, whose lysosomal clearance is not enhanced by rapamycin or nutrient deprivation.

Results

ATZ polymers are delivered to LAMP1/RAB7-positive endolysosomes for clearance

To understand lysosomal clearance of proteasome-resistant ATZ polymers, we first identified the degradative organelle by transiently

inhibiting lysosomal activity with bafilomycin A1 (BafA1; Klionsky *et al*, 2008). Confocal laser scanning microscopy (CLSM) of mouse embryonic fibroblasts (MEF) expressing HA-tagged ATZ shows that in cells exposed to BafA1 ATZ accumulates in endolysosomes (EL, as defined in Huotari & Helenius, 2011) that display LAMP1 [Fig 1A (mock-treated cells) vs. B (cells exposed to BafA1) and D] and RAB7 (Fig EV1) at the limiting membrane. The ATZ accumulating in inactive endolysosomes is decorated both with the anti-HA (Fig 1B, Inset HA) and with the 2C1 antibody (Inset 2C1), which is specific for the polymeric form of ATZ (Fig EV2A; Miranda *et al*, 2010). The wash-out of BafA1 readily re-establishes the clearance of polymeric ATZ as shown by the disappearance of the ATZ-specific signal in the LAMP1-positive organelles (Fig 1C, Insets, D). Biochemical analyses where the intracellular level of ATZ polymers immunoprecipitated with the 2C1 antibody from cell lysates is checked in Western blots (WB) confirm the increase in the polymer level on cell exposure to BafA1 (Fig 1E, lane 1 vs. 2, F) and its return to steady-state level 4 h after BafA1 wash-out (Fig 1E, lane 3, F). All in all, LAMP1-positive endolysosomes are the degradative organelles, where polymeric ATZ is delivered from the ER for clearance. These organelles are also visible in non-transfected cells [e.g., cells in the upper left and right corners, Fig 1B, panels LAMP1, Merge (HA), and Merge (2C1)]. This shows that their formation is not induced by the luminal expression of proteasome-resistant misfolded polypeptides such as ATZ.

Another disease-causing variant of the SERPINA1 gene, the folding-defective AT variant NHK, is also retained in the ER lumen. At steady state, NHK and ATZ are present at similar intraluminal levels based on the intensities of the HA signal determined in cytofluorimetry and by WB of total cell lysates (Fig EV2A and B). However, in contrast to ATZ (Fig EV2A, second panel), NHK does not form polymers as revealed by the absence of 2C1 immunoreactivity (third panel). NHK also does not accumulate within LAMP1-positive endolysosomes on lysosomal inactivation (Fig EV2C, BafA1). In fact, NHK is eventually dislocated across the ER membrane to be degraded by cytosolic proteasomes (Liu *et al*, 1999). Thus, delivery to endolysosomes for clearance is not a common fate of misfolded proteins generated in the ER, most of which are degraded by ER-associated degradation (ERAD; Guerriero & Brodsky, 2012; Pisoni & Molinari, 2016). It rather occurs to remove proteasome-resistant species (Teckman & Perlmutter, 2000; Kamimoto *et al*, 2006; Fujita *et al*, 2007; Ishida *et al*, 2009; Kroeger *et al*, 2009; Gelling *et al*, 2012; Houck *et al*, 2014), polymeric ATZ being a paradigmatic example.

Figure 1. Reversible accumulation of polymeric ATZ within LAMP1-positive endolysosomes on acute lysosomal inhibition.

- A Intracellular localization of total (HA) and polymeric ATZ (2C1) in WT MEF mock-treated, confocal laser scanning microscopy (CLSM).
 B Same as (A) for MEF exposed to 50 nM BafA1 for 12 h.
 C Same as (B), 4 h after BafA1 wash-out.
 D Quantification of ATZ-positive, LAMP1-positive endolysosomes (EL) ($n = 13, 10, 11$ cells, respectively). One-way ANOVA and Dunnett's multiple comparisons test, $^{ns}P > 0.05$, $^{****}P < 0.0001$.
 E ATZ polymers immunoprecipitated from lysates of WT MEF mock-treated (lane 1), incubated for 12 h with BafA1 (lane 2) and 4 h after BafA1 wash-out (lane 3). Immunoprecipitation (IP) of ATZ polymers with polymer-specific 2C1 antibody, transfer on PVDF membrane, revealed with anti-HA antibody on Western blot (WB).
 F Quantification of (E), $n = 3$, mean \pm SEM. Unpaired two-tailed t -test, $^{ns}P > 0.05$, $^{*}P < 0.05$.
 G–K Same as (B) in WT MEF, in cells exposed to 20 mM CST and in *Cnx-*, *Crt-*, and *ERp57-KO* MEF.
 L Quantification of ATZ-positive EL ($n = 10, 9, 11, 10, 11$ cells, respectively). One-way ANOVA and Dunnett's multiple comparisons test, $^{ns}P > 0.05$, $^{****}P < 0.0001$.

Data information: Scale bars: 10 μ m.

Source data are available online for this figure.

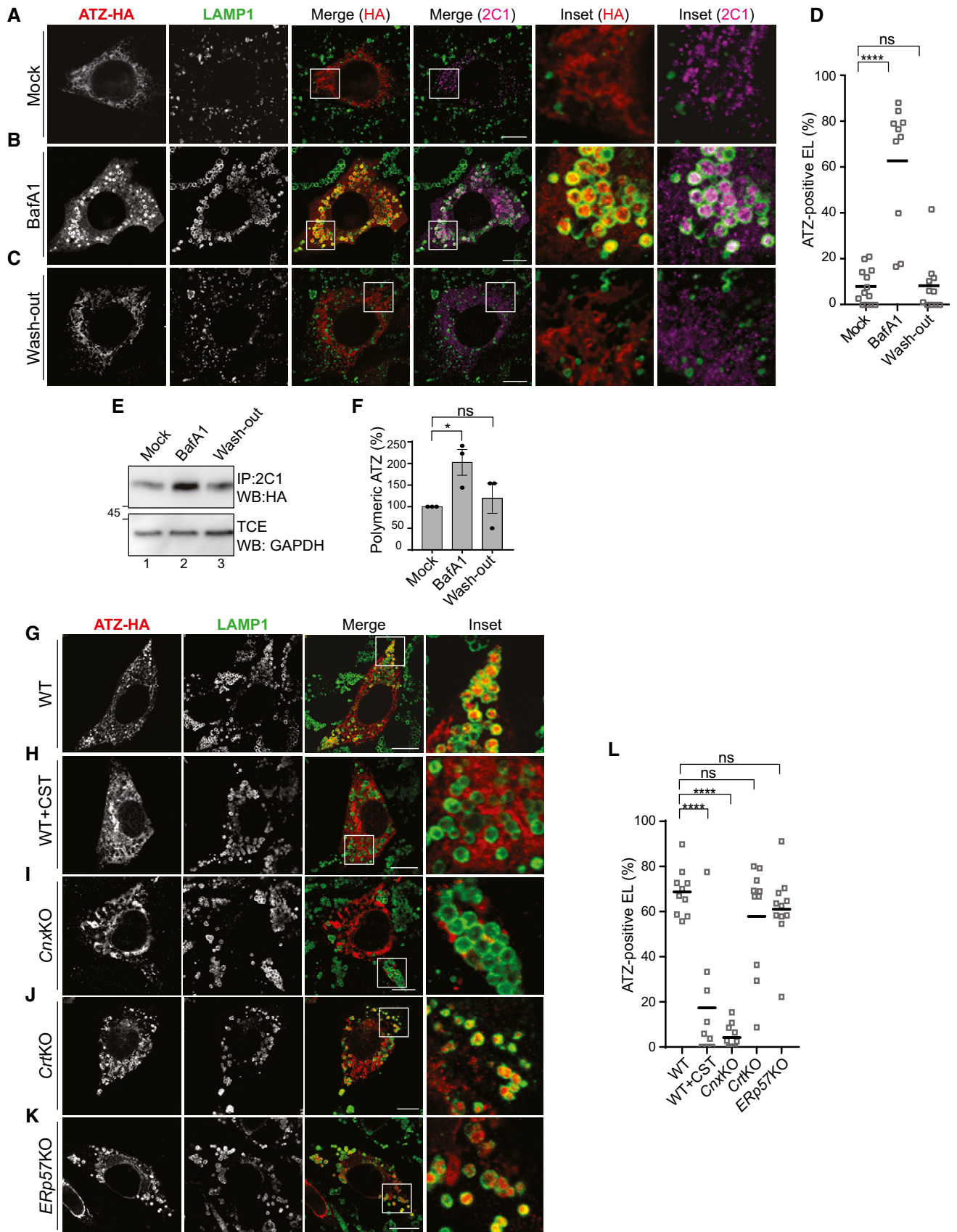


Figure 1.

Figure 2. Disposal of polymeric ATZ requires a functional LIR domain of FAM134B.

- A HEK293 cells transfected with empty vector (lanes 1, 6), ATZ-HA (2, 7), FAM134B-V5 (3 and 8), FAM134B-V5 and ATZ-HA (4, 9), or FAM134BLIR-V5 and ATZ-HA (5, 10), incubated for 6 h with 100 nM BafA1 and then treated with the cross-linker DSP before lysis as described in Materials and Methods. Lanes 1–5, WB of the total cell extract (TCE); lanes 6–10, WB of anti-V5 immunoprecipitates to isolate complexes containing ectopically expressed FAM134B or FAM134BLIR. The membranes were probed with anti-V5 (upper panels), anti-CNX, anti-HA, and anti-LC3 antibodies.
- B Quantification of LC3 co-precipitating with FAM134B-V5 (A, lanes 8 and 9). Mean \pm SEM, $n = 3$, unpaired two-tailed t -test, $*P < 0.05$.
- C Same as Fig 1B, WT MEF. Scale bar: 10 μ m.
- D Ectopic expression of FAM134BLIR in WT MEF inhibits ATZ delivery to endolysosomes. Scale bar: 10 μ m.
- E, F Distribution of gold-labeled ATZ-HA by IEM in BafA1-treated WT MEF and WT MEF overexpressing FAM134BLIR, respectively. EV, ER-derived vesicles, red arrowheads; EL, endolysosome.
- G Quantification of ATZ-gold density of (E, F) ($n = 75$ and 79 EL, respectively). Unpaired two-tailed t -test, $****P < 0.0001$.
- H Max projection of the same cell as in (D) after deconvolution. Insets show orthogonal section of select regions. Scale bar: 10 μ m.
- I Decay of ATZ polymers (CHX chase, upper panel) immunoprecipitated with the polymer-specific 2C1 antibody (visualized with anti-HA in WB) in HEK293 cells mock-transfected (lanes 1–4) or expressing FAM134BLIR-V5 (lanes 5–8). Middle panel, expression of FAM134BLIR-V5 assessed by WB; lower panel, loading control.
- J Quantification of (I) (Mean \pm SEM, $n = 3$, unpaired two-tailed t -test, $*P < 0.05$).
- K Flow cytometry analysis of ATZ-HA polymer levels in MEFs mock-treated, exposed to BafA1, and co-expressing FAM134LIR. MFI: mean fluorescence intensity (Mean \pm SEM, $n = 5$, unpaired two-tailed t -test, $^{ns}P > 0.05$, $**P < 0.01$, $****P < 0.001$).

Source data are available online for this figure.

Delivery of polymeric ATZ to endolysosomes requires the ER lectin CNX

The involvement of ER-resident chaperones in selection of folding-defective polypeptides for ERAD is well understood (Guerriero & Brodsky, 2012; Pisoni & Molinari, 2016). In contrast, their involvement in selection of proteasome-resistant aberrant proteins for lysosomal clearance is not studied. The only exception, to the best of our knowledge, shows that pharmacologic inactivation of the calnexin (CNX)/calreticulin (CRT)/Erp57 chaperone system with the plant alkaloid castanospermine (CST; Elbein, 1991; Hebert *et al*, 1995) prevents lysosomal delivery and disposal of GnrHR_{E90K} (Houck *et al*, 2014). The membrane-bound lectin chaperone CNX, its soluble and functional homolog CRT, and the associated oxidoreductase Erp57 catalyze oxidative and reductive reactions during polypeptide folding and unfolding in the ER (Caramelo & Parodi, 2007). It has therefore been speculated that their intervention in lysosomal clearance is required to attain a GnrHR_{E90K} structure competent for lysosomal delivery (Houck *et al*, 2014).

As reported for GnrHR_{E90K}, CST also abolishes delivery of ATZ to LAMP1-positive endolysosomes (Fig 1G vs. H and L). Our tests in cells lacking CNX reveal defective delivery of ATZ to the endolysosomes (Fig 1I and L). Ablation of CRT (Fig 1J and L) or Erp57 (Fig 1K and L) has in contrast no consequence. We have extensively studied ER-chaperone-assisted protein biogenesis and clearance. The folding machinery is highly redundant and pharmacologic inactivation of the CNX/CRT/Erp57 chaperone system on cell exposure to CST modestly impact on folding efficiency for most cellular proteins (Denzel *et al*, 2002; Molinari *et al*, 2004, 2005; Pieren *et al*, 2005; Soldà *et al*, 2006, 2007). On the same line, less invasive approaches, such as the ablation of either CNX or CRT or Erp57, are efficiently compensated in culture cells by the activation of surrogate pathways (Soldà *et al*, 2006). For that reason, we consider unlikely that the block of ATZ delivery to the endolysosomes on CST treatment, which is recapitulated in cells lacking CNX, results from a specific involvement of CNX in attainment of a delivery-competent ATZ structure. Consistently, the generation of ATZ polymers is unperturbed in cells exposed to CST or lacking CNX (Fig EV2A, fourth and fifth panels, respectively). Rather, we

hypothesize a role of CNX as a membrane-bound receptor that segregates ATZ polymers in ER subdomains to be delivered to endolysosomes for clearance.

ATZ expression favors formation of a CNX:FAM134B:LC3II complex

Our hypothesis that CNX participates in a membrane receptor to segregate ATZ polymers from the ER lumen is corroborated by recent literature indicating CNX as an interactor of FAM134B (Grumati *et al*, 2017). FAM134B is a recently characterized ER-phagy receptor (i.e., an ER-resident, LC3-binding protein involved in ER fragmentation and delivery of ER subdomains to LAMP1-positive endolysosomes for clearance; Fregno & Molinari, 2018; Loi *et al*, 2018). The biological significance of CNX association with FAM134B is not known, as this interaction is not required for FAM134B-regulated, ER stress-induced, or starvation-induced ER-phagy (unpublished and Fumagalli *et al*, 2016; Khaminets *et al*, 2015). Immunoprecipitation of epitope-tagged FAM134B from lysates of HEK293 cells confirms the association of endogenous CNX and of endogenous LC3II (Fig 2A, lane 8). Significantly, the co-expression of ATZ-HA substantially enhances the co-precipitation of endogenous CNX and LC3II with V5-tagged FAM134B (Fig 2A, lane 9, B). FAM134BLIR, where the LC3-binding function has been inactivated on replacement of six residues in the cytosolic LC3-interacting region (LIR) of FAM134B (⁻⁴⁵³DDFELL₄₅₈ to ⁻⁴⁵³AAAAAA₄₅₈), also associates with ATZ and CNX but, as expected, it does not engage LC3 (Fig 2A, lane 10). Under these experimental conditions, i.e., ectopic expression of FAM134BLIR, endolysosomal delivery of ATZ is blocked (Fig 2C vs. D). Our analyses by immuno-electron microscopy (IEM, immunogold-labeled ATZ, Fig 2E–G) and by CLSM (Fig 2H) reveal that ATZ is released in ER-derived vesicles (red arrowheads in Fig 2F, EV in the insets of Fig 2H and see below). However, the ATZ-containing EV remain dispersed in the cytosol, thus failing to release their content within endolysosomes (Fig 2C vs. D, E vs. F and G). As a consequence, clearance of polymeric ATZ is substantially delayed as determined by a cycloheximide (CHX) chase (Fig 2I and J), thus resulting in intracellular accumulation of ATZ polymers at levels comparable to those obtained by cell exposure

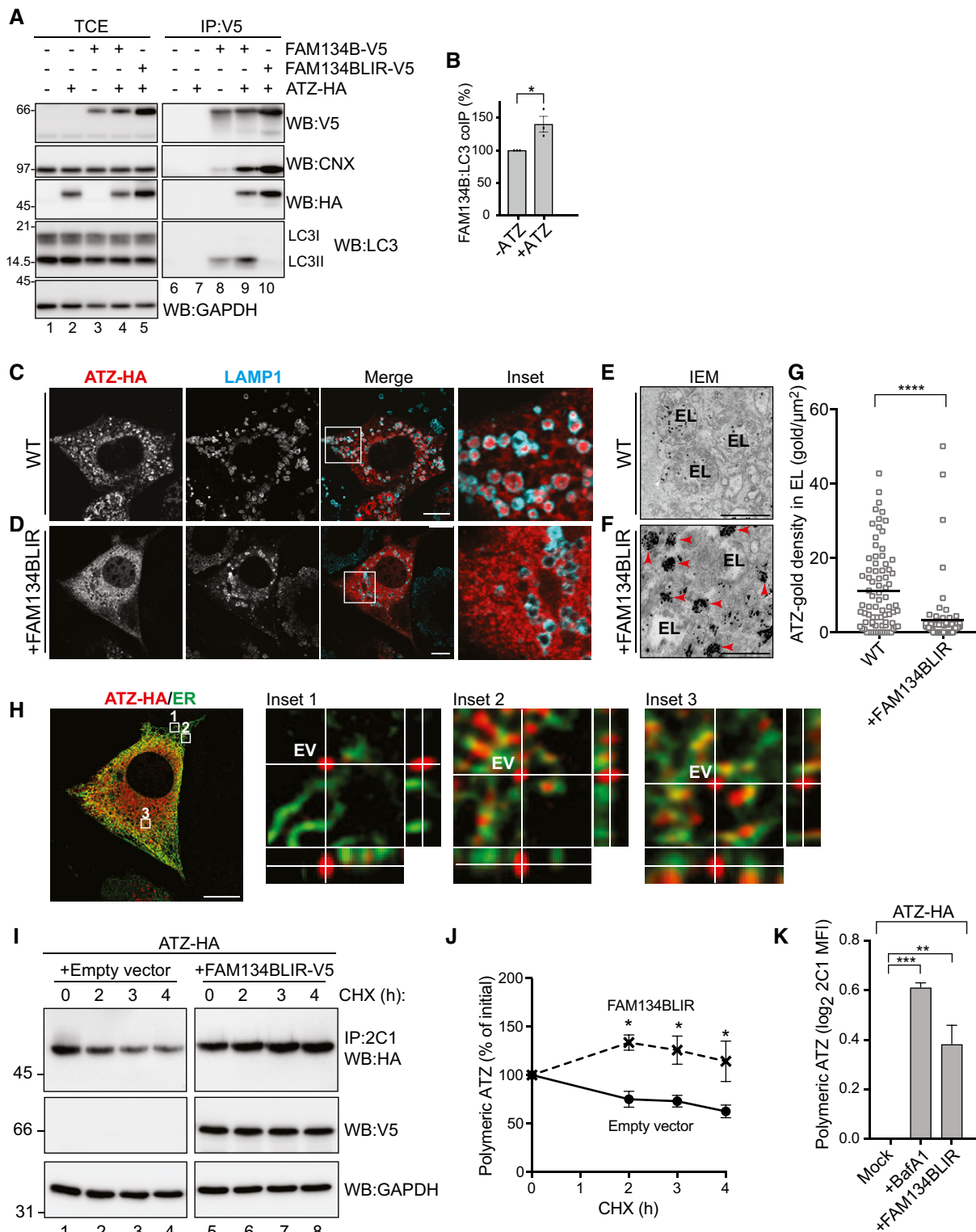


Figure 2.

to BafA1 as quantified by cytofluorimetry (Fig 2K). All in all, the LC3-binding function of FAM134B is dispensable for formation of a complex with CNX and ATZ and for the generation of ATZ-containing EV, but it is required to target EV to

endolysosomes where their content must be released for clearance. We postulate, and show below, that FAM134B association with LC3 promotes EV docking to the endolysosomal membrane that precedes membrane:membrane fusion events eventually

leading to delivery of polymeric ATZ within endolysosomes for clearance.

FAM134B is required for delivery of polymeric ATZ to endolysosomes

To confirm the role of FAM134B in clearance of proteasome-resistant polymeric ATZ from the ER lumen, delivery of ATZ polymers within endolysosomes was analyzed in WT MEF and in MEF ablated of FAM134B by use of CRISPR/Cas9 genome editing technology (Fig 3A). CLSM analyses confirm delivery of ATZ in LAMP1-positive endolysosomes in WT MEF (Fig 3C and F), which is compromised in FAM134B-ablated cells (Fig 3D and F). Deletion of SEC62 (Fig 3B), another ER-resident, LC3-binding protein that regulates ER-phagy after termination of an ER stress (Fumagalli *et al*, 2016; Fregno & Molinari, 2018; Loi *et al*, 2018) does not perturb endolysosomal delivery of ATZ polymers for clearance (Fig 3E and F).

Delivery of polymeric ATZ to the endolysosomes requires a functional LC3 lipidation machinery

FAM134B associates with lipidated LC3II. The LC3-binding function of FAM134B is required to deliver ER fragments within autophagolysosomes during ER-phagy (Khaminets *et al*, 2015) and for delivery of ATZ polymers to endolysosomes for clearance (Fig 2). To assess whether the LC3 lipidation machinery participates in clearance of ATZ polymers, we monitored their delivery to LAMP1-positive endolysosomes in MEF with defective LC3 lipidation due to ablation of ATG4B (Marino *et al*, 2010) or ATG7 (Komatsu *et al*, 2005; Fig EV3A and B). Indeed, lysosomal delivery of ATZ such as occurs in WT MEF (Fig 4A, Insets, I) is defective in cells lacking ATG4B (Fig 4B and I) or ATG7 (Fig 4C and I). On the same line, SAR405, a specific inhibitor of VPS34 that prevents LC3 lipidation and autophagosome biogenesis (Ronan *et al*, 2014; Bento *et al*, 2016), fully blocks delivery of proteasome-resistant misfolded ATZ from the ER lumen to the endolysosomes (Fig EV4).

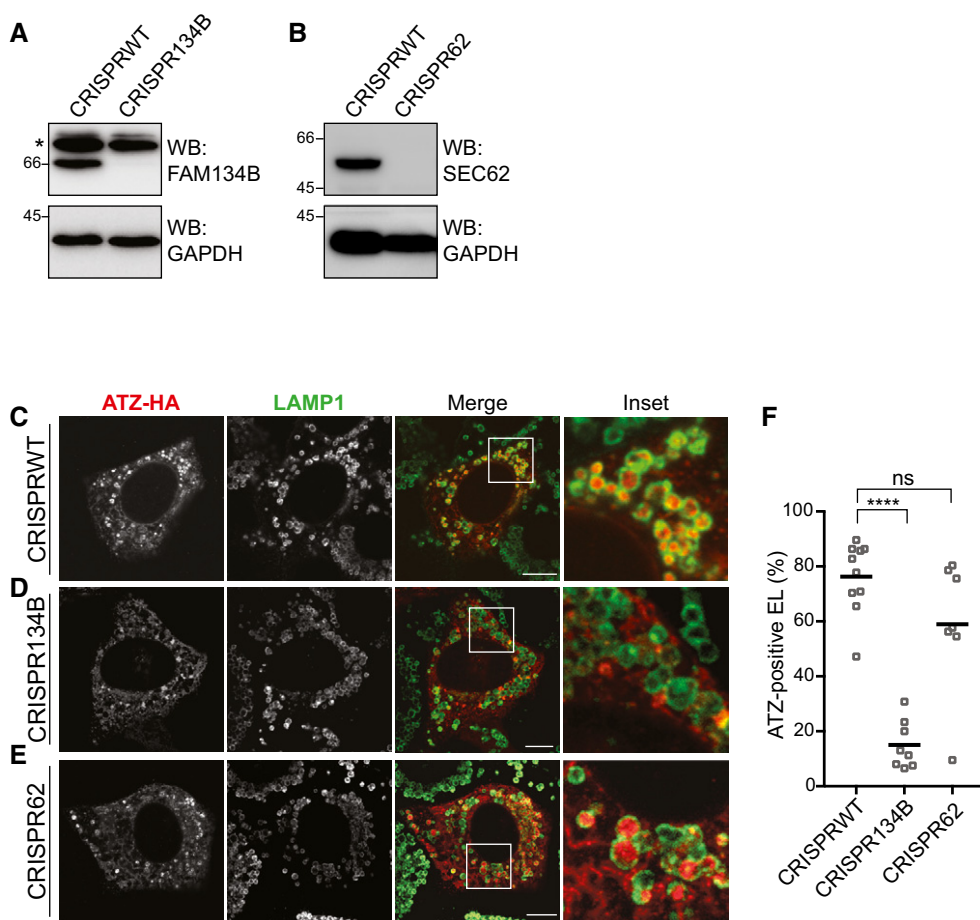


Figure 3. Delivery of polymeric ATZ to LAMP1-positive endolysosomes and clearance of ATZ polymers requires FAM134B.

A WB analysis showing KO efficiency for CRISPR134B MEF. Asterisks, cross-reacting bands.

B Same as (A) for CRISPR62 MEF.

C–E Same as Fig 1B in CRISPR WT MEF, CRISPR134B MEF, CRISPR62 MEF, respectively. Scale bars: 10 μ m.

F Quantification of (C–E) ($n = 10, 8, 7$ cells, respectively). One-way ANOVA and Dunnett's multiple comparisons test, $^{ns}P > 0.05$, $^{****}P < 0.0001$.

Source data are available online for this figure.

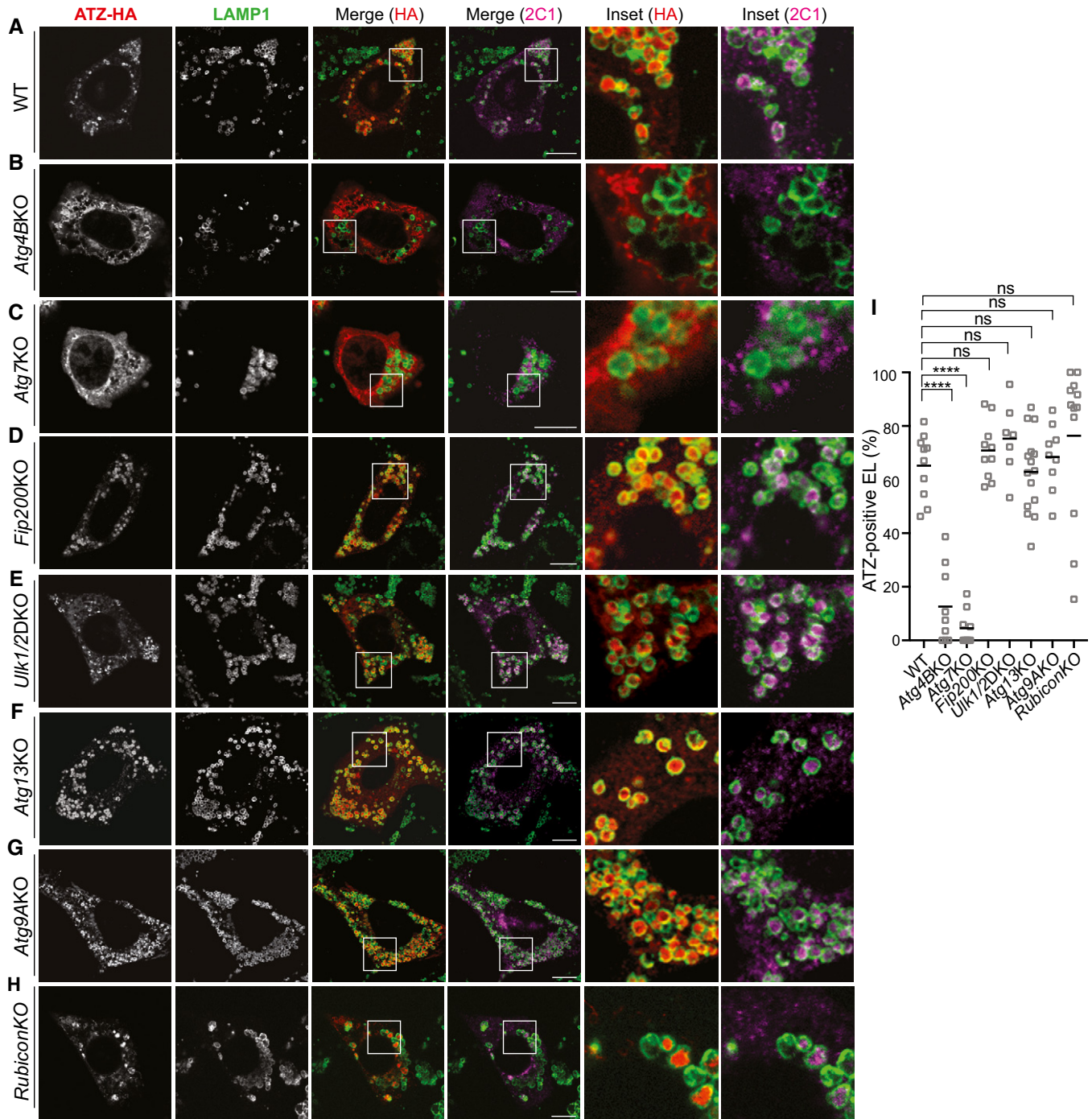


Figure 4. Delivery of polymeric ATZ to endolysosomes in cells lacking LC3 lipidation or autophagosome biogenesis.

A–H Intracellular localization of LAMP1-positive EL, total (HA), and polymeric (2C1) ATZ in WT MEF exposed to BafA1 for 12 h (A); in *Atg4BKO* MEF (B); in *Atg7KO* MEF (C); in *Fip200KO* MEF (D); in *Ulk1/2* double-KO MEF (E); in *Atg13KO* MEF (F); in *Atg9AKO* MEF (G); in *RubiconKO* MEF (H). Scale bars: 10 μ m.

I Quantifications of (A–H) ($n = 10, 9, 9, 10, 7, 15, 9, 12$ cells). One-way ANOVA and Dunnett's multiple comparisons test, ^{ns} $P > 0.05$, ^{****} $P < 0.0001$.

Delivery of polymeric ATZ to the endolysosomes does not require a functional autophagosome biogenesis machinery

So far, our data on endolysosomal delivery of ATZ polymers echo the findings on nutrient deprivation-induced, FAM134B-dependent,

and LC3-dependent ER-phagy. Yet, nutrient deprivation-induced ER-phagy critically depends on FIP200 (Khaminets *et al*, 2015), a core component of the ULK kinase complex that is required for the generation of autophagosomes that eventually capture and deliver ER fragments to the lysosomal compartments (Hara *et al*, 2008;

Hosokawa *et al.*, 2009; Smith *et al.*, 2018). Strikingly, our analyses reveal that the FAM134B-dependent ATZ delivery to endolysosomes is not affected in cells lacking FIP200 (Fig 4D and I, and EV3B) or other components of the autophagosome biogenesis machinery such as ULK1 and ULK2 (Fig 4E and I, and EV3A and B), ATG13 (Fig 4F and I, and EV3A and B) or ATG9 (Fig 4G and I, and EV3A and B; Saitoh *et al.*, 2009; Shang *et al.*, 2011; McAlpine *et al.*, 2013; Bento *et al.*, 2016; Kaizuka & Mizushima, 2016; Hurley & Young, 2017; Kakuta *et al.*, 2017). Thus, defective autophagosome biogenesis impairs several types of receptor-mediated ER-phagy (Khaminets *et al.*, 2015; Grumati *et al.*, 2017; Fregno & Molinari, 2018; Loi *et al.*, 2018; Smith *et al.*, 2018) and conventional macroautophagy (Fig EV3B; Hara *et al.*, 2008; Hosokawa *et al.*, 2009; Kakuta *et al.*, 2017). However, it does not affect delivery of proteasome-resistant ATZ polymers to endolysosomes for clearance. Dispensability of ULK1/ULK2 (with requirement of the LC3 conjugation machinery) has previously been reported, for example, for LC3-associated phagocytosis (LAP; Martinez *et al.*, 2015). Like delivery of polymeric ATZ to endolysosomes, LAP does not require the activity of the pre-initiation complex and autophagosome biogenesis (ULK1/2, ATG13, FIP200 are dispensable for both pathways, the LC3 conjugation complex is required for both pathways). However, dispensability of Rubicon (Fig 4H and I, and EV3A) distinguishes ATZ clearance from LAP.

Vesicular delivery of proteasome-resistant ATZ from the ER to endolysosomes

To better appreciate the intracellular fate of ATZ, we performed ultrastructural analyses by IEM in WT MEF, which revealed the presence of ATZ in the ER (Fig 5A, C, D and F, Movie EV1), its segregation in ER subdomains (ES, Fig 5D and F, Movie EV1) and in single-membrane, ER-derived vesicles (EV) that dock onto endolysosomes (EL) and deliver ATZ within their lumen (Fig 5A, B, E and F, Movie EV1, red asterisks in Fig 5B and E show the opening at the contact sites between EV and EL). Autophagosomes identified in correlative light-electron microscopy for their double-membrane heavily decorated with GFP-LC3 (green fluorescence and immunogold labeling, Fig 5G and insets) do not contain ATZ, which is stained in red (Fig 5G). This is consistent with dispensability of the autophagosome biogenesis machinery for delivery of ATZ to the endolysosomes (Fig 4D–G and I).

ATZ is delivered within endolysosomes in conjunction with ER luminal, but not ER membrane proteins

To elucidate the sequential steps of delivery of proteasome-resistant polymeric ATZ from the ER lumen to LAMP1-positive endolysosomes, we set up an original HaloTag pulse-chase protocol. HaloTag is an inactive bacterial hydrolase, whose active site has been modified to facilitate covalent and irreversible binding of synthetic ligands, including cell-permeable ligands that are coupled to fluorescent probes (England *et al.*, 2015). We first validated that the HaloTag, which was placed at the N-terminus of ATZ, did not affect polymerization and lysosomal clearance of ATZ (Dickens *et al.*, 2016 and Fig EV5A). We then employed the following pulse-chase setup: WT MEF expressing HaloTag-ATZ were incubated for 30 min with a cell-permeable “black ligand” (i.e., 6-Chlorohexanol) to quench

fluorescent detection of the pre-existing pool of HaloTag-ATZ. Next, we replaced the “black ligand” by a cell-permeable fluorescent HaloTag ligand to label newly synthesized HaloTag-ATZ for 15 min (fluorescent pulse). Finally, we washed out the fluorescent ligand and replaced it with the “black ligand” again to interrupt fluorescent labeling of HaloTag-ATZ (chase). As such, we followed the fate of the cohort of fluorescently pulse-labeled HaloTag-ATZ for various chase times: 0, 30, 120, 180, and 300 min (Fig 6A–F). Early upon being synthesized, fluorescently labeled HaloTag-ATZ co-localized with the luminal ER marker (superfolder) sfGFP-KDEL within the ER (Fig 6A and B, M1, M2, 0–30 min of chase and Fig 6G). Interestingly, the co-localization of HaloTag-ATZ with sfGFP-KDEL persisted throughout the 300 min of chase (Fig 6G and H) and was observed in the ER (Fig 6A and B, M1–M3), in the EV (M4) and within the LAMP1-positive endolysosomes (M5, M5A, M5B, and Fig EV5B). In mock-transfected cells or in cells expressing the folding-defective protein NHK, which relies on the UPS for clearance, delivery of sfGFP-KDEL from the ER into LAMP1-positive endolysosomes is below detection level (Fig EV5C and D). Thus, accumulation of proteasome-resistant ATZ in the ER lumen activates (or strongly enhances) a vesicular transport pathway that delivers ATZ polymers and ER luminal content within endolysosomes.

In contrast, co-localization of HaloTag-ATZ with markers of the ER membrane such as CNX and CLIMP63 is seen only early after pulse-labeling, when HaloTag-ATZ is still in the ER (Fig 6C and D, M6, M7 for CNX; 6E and F, M11, M12 for CLIMP63). At later chase times, co-localization is progressively lost (Fig 6C and D, M8, M9, M10, M10A, M10B for CNX; Fig 6E and F, M13, M14, M15, M15A, M15B for CLIMP63 and Fig 6G). All in all, ATZ (Fig 6, M5A, M10A, M15A) and sfGFP-KDEL (Fig 6, M5B) are co-delivered within LAMP1-positive endolysosomes. The ER membrane markers CNX (Fig 6, M10B) and CLIMP63 (Fig 6, M15B) are not. These data further highlight the mechanistic distinction with receptor-regulated ER-phagy pathways, which are activated by nutrient deprivation or ER stress to deliver ER fragments (i.e., luminal and membrane ER proteins) within lysosomal compartments (Khaminets *et al.*, 2015; Fumagalli *et al.*, 2016; Grumati *et al.*, 2017; Fregno & Molinari, 2018; Loi *et al.*, 2018; Smith *et al.*, 2018).

The ER-resident SNARE STX17 and the endolysosomal SNARE VAMP8 are required for ATZ delivery to endolysosomes for clearance

The observation of fusion events occurring between single-membrane-bound ER-derived vesicles containing ATZ and endolysosomes (Fig 5) prompted us to assess the involvement in this catabolic pathway of the ER-resident SNARE STX17, which is involved in smooth ER membrane dynamics and fusion events (Steggmaier *et al.*, 2000) and of the endolysosomal SNARE VAMP8 (Ktistakis & Tooze, 2016). To this end, we generated cells lacking STX17 or VAMP8 (Fig 7A and B) using the CRISPR/Cas9 genome editing technology. In contrast to WT MEF, in which ATZ polymers accumulate in inactive endolysosomes (Fig 7C, Insets, F and G), STX17-ablated MEF display ATZ-containing vesicles (EV) that peripherally dock onto the endolysosomal (EL) membrane but fail to release their content in the EL lumen (Fig 7D, Insets, F and H). Likewise, deletion of VAMP8 abolishes ATZ delivery within endolysosomes (Fig 7E, F and I). Notably, starvation-induced

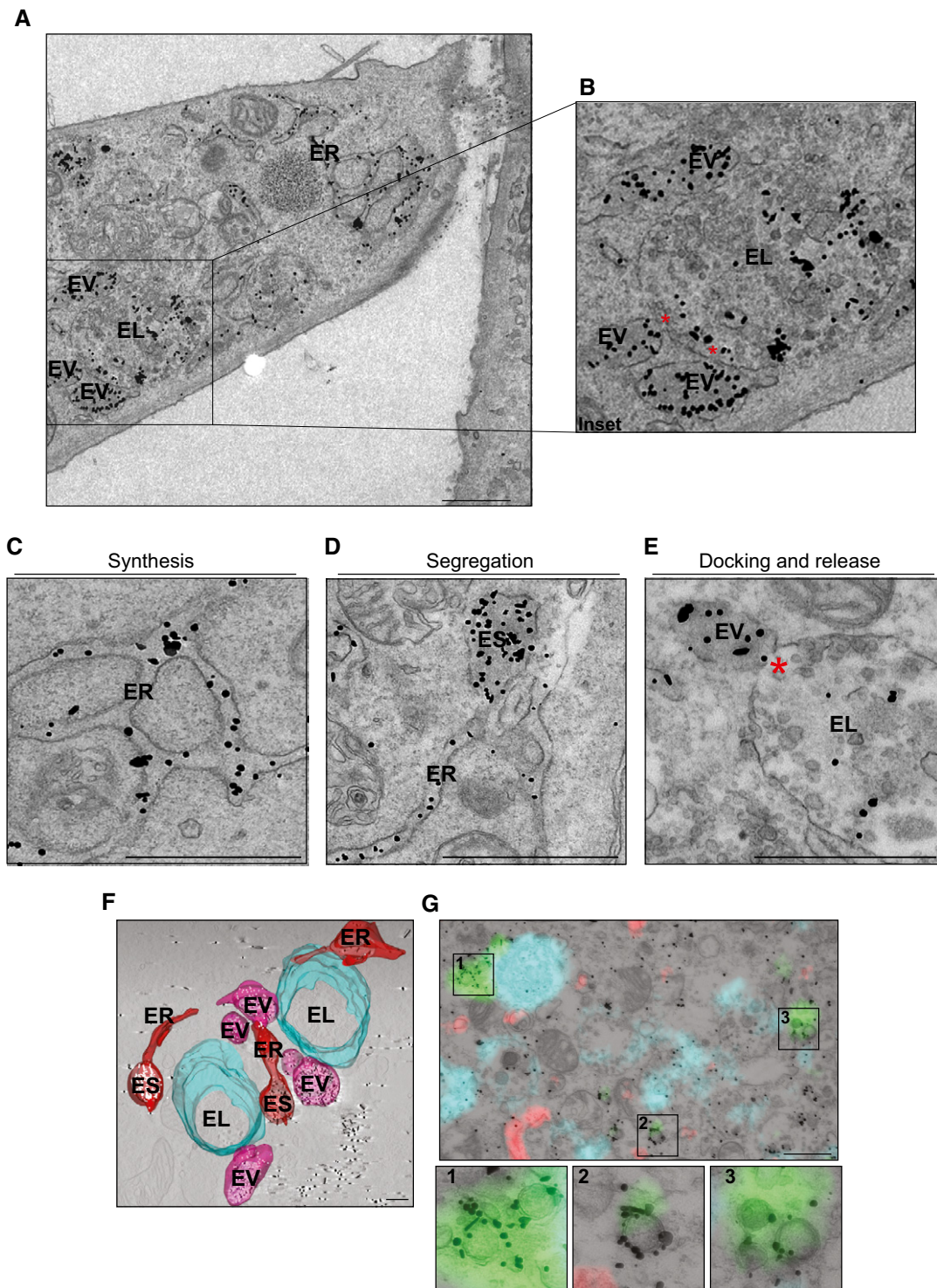


Figure 5. Dissecting ATZ delivery to LAMP1-positive endolysosomes.

A Distribution of gold-labeled ATZ-HA by IEM in WT MEF exposed to BafA1 (the cell on the right is not transfected, as specificity control for gold labeling). ER, endoplasmic reticulum; EV, ER-derived vesicle; EL, endolysosomes. Scale bar: 1 μ m.

B Inset of A. Red asterisks show site of EV:EL membranes fusion.

C–E Distribution of gold-labeled ATZ-HA by IEM in WT MEF. ES, ER subdomains. Red asterisk shows site of EV:EL membranes fusion. Scale bar: 1 μ m.

F 3D visualization by means of electron tomography of organelles containing gold-labeled ATZ-HA (visualized as white dots, see Movie EV1). ES, ER subdomains. Scale bar: 500 nm.

G CLEM showing ATZ (red), LAMP1-positive EL (cyan), and GFP-derived fluorescence (green) in correspondence to heavily labeled vesicles, which were identified as autophagosomes for their double membrane (insets 1–3). GFP-LC3 was also stained by immunogold. Scale bar: 1 μ m.

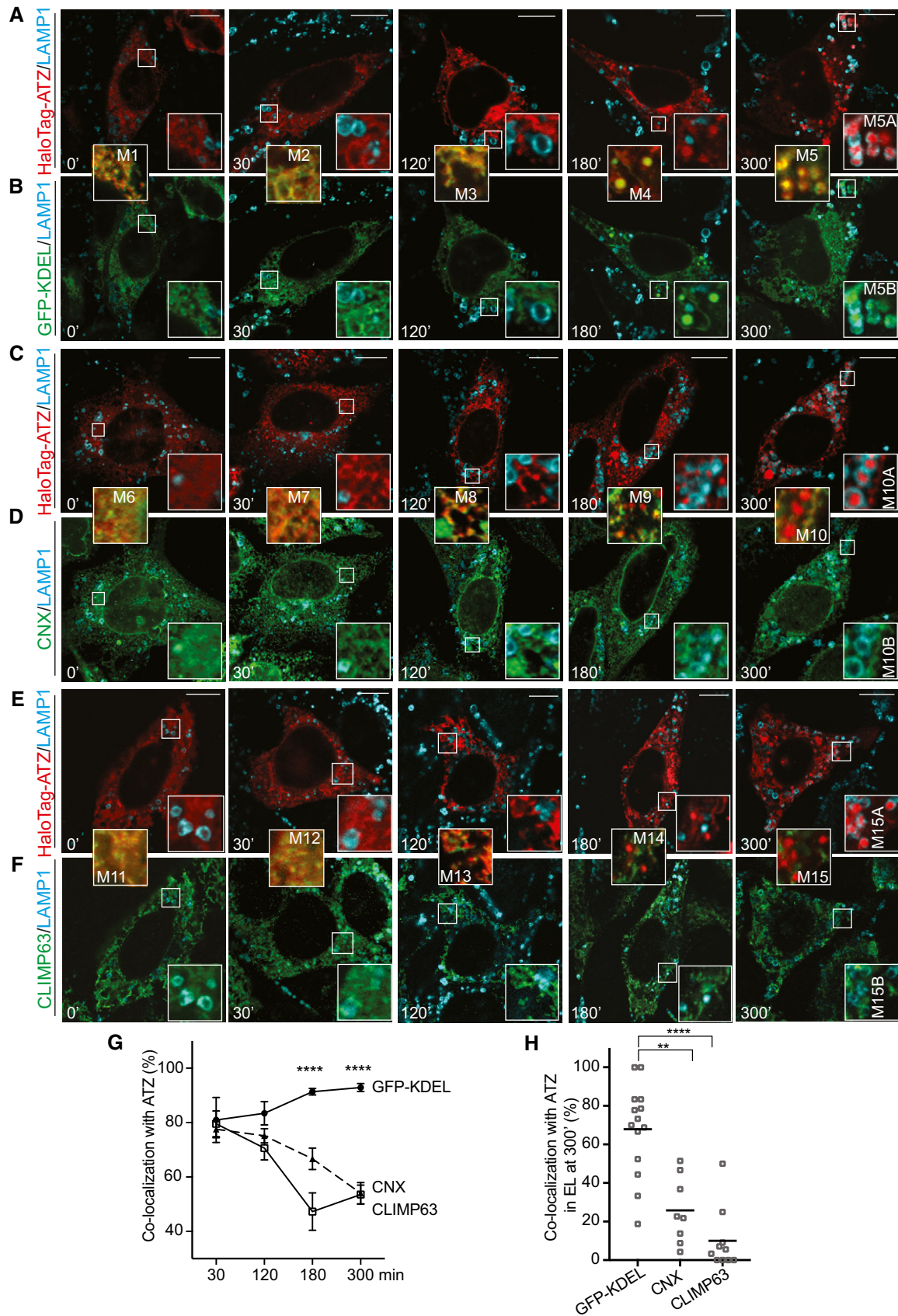


Figure 6.

Figure 6. Time course by HaloTag pulse-chase of ATZ delivery to endolysosomes.

- A, B Triple staining of cells with LAMP1 (cyan), HaloTag-ATZ (red), and the luminal ER marker sfGFP-KDEL (green).
 C, D Same as (A, B), with CNX as ER membranes marker.
 E, F Same as (A, B), with CLIMP63 as ER membranes marker.
 G Quantification of ER markers and HaloTag-ATZ co-localization in time (sfGFP-KDEL $n = 10, 10, 12, 13$, CNX $n = 8, 10, 9, 8$, CLIMP63 $n = 8, 10, 6, 10$ cells for corresponding time points). Mean \pm SEM, unpaired two-tailed t-test, **** $P < 0.0001$.
 H Quantification of double-positive endolysosomes at 300' (ATZ:sfGFP-KDEL $n = 14$, ATZ:CNX $n = 8$, ATZ:CLIMP63 $n = 10$ cells. One-way ANOVA and Dunnett's multiple comparisons test, ** $P < 0.01$, **** $P < 0.0001$).
- Data information: Scale bars 10 μ m.

FAM134B-regulated ER-phagy proceeds normally in cells lacking STX17 as is evident from the delivery of CLIMP63 into the LAMP1-positive endolysosomes (Fig EV5E–G).

FAM134B:LC3II foci at the ER-derived vesicles/endolysosomes interface

To monitor the formation of FAM134B:LC3II complexes, we used a bi-partite split GFP complementation assay (Cabantous *et al*, 2005; Cieri *et al*, 2018). We tagged the C-terminus of FAM134B with the eleventh β strand of GFP (T₁₁) and the N-terminus of LC3 with the remaining portion of GFP (GFP_{1–10}), which lacks fluorescence ability (Cabantous *et al*, 2005; Cieri *et al*, 2018). Foci of GFP reconstitution thus report on active FAM134B:LC3II complexes, which co-localize with ATZ-HA and cluster at the limiting membrane of endolysosomes (Fig 7J, arrowheads in Insets). We confirmed by correlative light-electron microscopy (CLEM) that foci of GFP reconstitution represent functional FAM134B:LC3II complexes (green and yellow signal in Fig 7K) that localize at the interface between ATZ-containing ER-derived vesicles (EV, red in Fig 7K) and LAMP1-positive endolysosomes (cyan in Fig 7K, where FAM134B-T₁₁ is also labeled with gold). These foci are absent in cells co-transfected with FAM134B-T₁₁ and non-lipidable GFP_{1–10}-LC3I (Fig EV5H). Thus, we conclude that localization of the FAM134B:LC3II complex at sites where ER-derived, ATZ transporting vesicles dock onto the endolysosomes is a prerequisite for the ensuing STX17/VAMP8-mediated fusion.

Discussion

Our analyses reveal that accumulation of proteasome-resistant ATZ polymers in the ER lumen (Fig 7L, step 1) activates a catabolic

process, where ATZ polymers are first segregated into ER subdomains under control of the ER lectin chaperone CNX (step 2) and then in single-membrane ER-derived vesicles with intervention of the ER-resident, LC3-binding protein FAM134B (step 3). FAM134B association with membrane-bound LC3II promotes EV docking to RAB7/LAMP1-positive endolysosomes (step 4). A subsequent membrane:membrane fusion event controlled by the ER-resident SNARE STX17 and the endolysosomal SNARE VAMP8 releases ATZ polymers within endolysosomes for clearance (step 5). We name this pathway ER-to-lysosome-associated degradation (ERLAD) to distinguish it from catabolic pathways named ER-phagy, where ER fragments whose production is enhanced upon nutrient deprivation or ER stresses are cleared from cells with the intervention of double-membrane autophagosomes (Khaminets *et al*, 2015; Fumagalli *et al*, 2016; Grumati *et al*, 2017; Fregno & Molinari, 2018; Loi *et al*, 2018; Smith *et al*, 2018). ERLAD shares with one of the ER-phagy pathways identified so far, namely with starvation-induced ER sheets turnover (Khaminets *et al*, 2015), the requirement of the LC3-binding, ER-resident protein FAM134B, and of the LC3 lipidation machinery. However, in sharp contrast with ER-phagy and other mTOR-dependent catabolic pathways, the autophagosome biogenesis machinery is dispensable for ERLAD. In ERLAD, ER-derived vesicles containing material to be removed from cells are not captured by autophagosomes but rather fuse with endolysosomes. Intriguingly, “non-autophagic clearance from the ER of aggregated proteins by direct conversion of ER cisternae into lysosomes” has been reported by Marilyn Farquhar over 25 years ago for aggregated β subunits of thyrotrophic hormone in the mouse thyroid gland (Noda & Farquhar, 1992). We believe that our characterization of the ERLAD pathway supports and offers a mechanistic explanation to these early observations.

Misfolded ATZ associates with FAM134B. The interaction is indirect since FAM134B does not display significant luminal domains

Figure 7. STX17 and VAMP8 are required for ATZ delivery within endolysosomes.

- A KO efficiency in CRISPR17 MEF.
 B Same as (A) for CRISPR8.
 C–E CLSM analysis of ATZ delivery to LAMP1-positive endolysosomes in BafA1-treated CRISPRWT MEF (C); in CRISPR17 MEF(D); in CRISPR8 MEF (E). Scale bars: 10 μ m.
 F Quantification of (C–E) ($n = 10, 10, 11$ cells, respectively). One-way ANOVA and Dunnett's multiple comparisons test, **** $P < 0.0001$.
 G–I Distribution of gold-labeled ATZ-HA by IEM in CRISPRWT MEF exposed to BafA1 (G); in CRISPR17 (H); in CRISPR8. (I). ER, endoplasmic reticulum; EV, ER-derived vesicles; EL, endolysosomes. Scale bars: 1 μ m.
 J GFP reconstitution in ATZ-HA-transfected CRISPR17 MEF expressing FAM134B-T₁₁ and GFP_{1–10}-LC3. Scale bar: 10 μ m.
 K Same as (J) by CLEM. ATZ-HA staining in red, LAMP1-positive endolysosomes in cyan. FAM134B:LC-induced GFP reconstitution in green. FAM134B in gold is shown. Scale bar: 1 μ m.
 L ERLAD schematics. 1. Synthesis and CNX-independent polymers formation; 2. CNX-regulated polymers segregation in ER subdomains (ES); 3. FAM134B-dependent (LIR-independent) formation of ER-derived vesicles (EV); 4. FAM134B:LC3II-mediated EV docking to RAB7/LAMP1-positive endolysosomes (EL); 5. STX17/VAMP8-controlled fusion of EV:EL membranes and polymers release in the EL lumen for clearance.

Source data are available online for this figure.

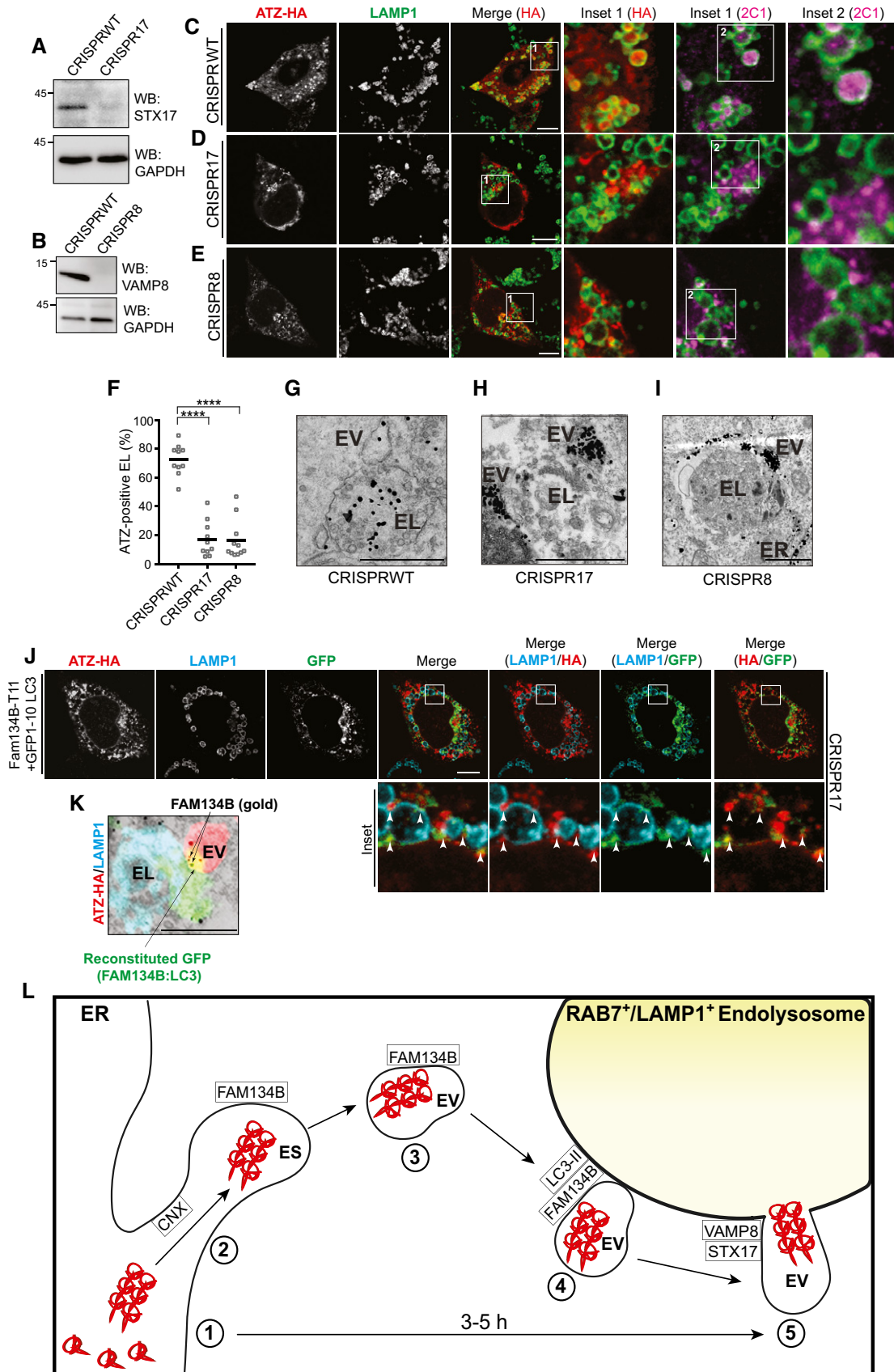


Figure 7.

and occurs via the FAM134B-interactor CNX. Apparently, the condensation of ATZ aggregates and the ensuing concentration of FAM134B in ER subdomains activate FAM134B to drive ER fragmentation. In ER-phagy, ER fragmentation seemingly requires the association of the cytosolic domain of FAM134B with LC3II possibly displayed at the membrane of growing phagophores (Khaminets *et al*, 2015). Not so in ERLAD, where inactivation of the FAM134B's LIR does not prevent generation of ATZ-containing ER-derived vesicles. However, these remain dispersed in the cytosol and fail to dock to and to release their content within endolysosomes. This, and the observation in CLEM that GFP reconstitution on formation of FAM134B:LC3II complexes occurs at the interface between endolysosomes and ATZ-containing ER-derived vesicles, lead us to speculate that FAM134B decorates the ER vesicles containing ATZ and that LC3 is lipidated on the target, endolysosomal membrane. How this is regulated is matter of future investigation.

An original HaloTag pulse-chase protocol used here for the first time allowed to monitor in CLSM the sequence of events that, with a half-time of about 3 h, lead newly synthesized ATZ to form proteasome-resistant polymers that are eventually delivered within endolysosomes for clearance (Fig 7L). These data reveal the progressive segregation of ATZ from the ER membrane marker proteins CNX and CLIMP63 that, as an additional difference with FAM134B-regulated ER-phagy, are not delivered within endolysosomes. The case of CNX (required for ATZ segregation and delivery within endolysosomes, but not itself transported to the degradative organelles) testifies a regulated dissociation of this lectin chaperone from ERLAD substrates (i.e., ATZ polymers). This reminds the regulated dissociation of CNX from folding-defective polypeptides to be cleared by ERAD, where CNX selects the misfolded polypeptides and these are eventually handed off to the BiP chaperone system before their dislocation across the ER membrane and proteasomal clearance (Molinari *et al*, 2005). For ERAD, interruption of misfolded polypeptides association with CNX that precedes clearance from the ER lumen is regulated by the progressive de-mannosylation of oligosaccharides displayed on misfolded polypeptides (Molinari *et al*, 2003; Oda *et al*, 2003; Olivari & Molinari, 2007). For ERLAD, this remains to be established.

There are clear genetic correlations between autophagy impairment and neurodegenerative diseases for which the root cause is the accumulation of proteasome-resistant aggregates and polymers in the cytosol (Menzies *et al*, 2017). Excitingly, rapamycin, rapalogs, and other small and non-small molecules that induce autophagic activity help to boost clearance of aggregates in various cellular and animal models of these types of disease. In fact, these strategies of enhancing autophagy are so promising that they are currently progressing into clinical validation (Menzies *et al*, 2017). There are also examples of proteasome-resistant inclusions in the ER lumen such as those formed by procollagen and dysferlin, whose degradation is reportedly enhanced upon macroautophagy activation (Fujita *et al*, 2007; Ishida *et al*, 2009). Based on our findings, we would argue that removal of these inclusions is likely regulated by ER-phagy and relies on autophagosome intervention. In contrast, rapamycin (Kroeger *et al*, 2009; Hidvegi *et al*, 2010), fasting (Teckman *et al*, 2002), or other classical macroautophagy activators are ineffective or even detrimental as therapeutic approaches both in cell lines and in mouse models for ATZ, other serpinopathies, and for the GnRHR_{E90K} (Teckman *et al*, 2002; Kroeger *et al*, 2009; Hidvegi

et al, 2010; Houck *et al*, 2014). Our data on vesicular delivery of ATZ polymers from the ER to endolysosomes and on dispensability of autophagosome intervention may explain why strategies that boost macroautophagy fail to induce clearance of ATZ and ATZ-like aggregates. In this context, the reported benefits on ATZ disposal of pharmacologic [e.g., carbamazepine (Chu *et al*, 2014; Hidvegi *et al*, 2010; Kroeger *et al*, 2009)] or genetic approaches [transcription factor EB (TFEB) gene transfer (Pastore *et al*, 2013)] should/could be ascribed to ill-defined consequences of the reduction in the inositol levels as a consequence of carbamazepine exposure, or to the enhanced number and function of lysosomes as a consequence of TFEB expression (Sardiello *et al*, 2009), respectively, rather than on induction of macroautophagy.

Finally, removal of misfolded proteins from the ER is crucial to maintain proteostasis. It is assumed that most aberrant polypeptides generated in the ER lumen are degraded by cytosolic 26S proteasomes by sequential processes collectively defined as ERAD. ERAD relies on dozens of ER-resident and cytosolic chaperones and enzymes that sequentially regulate interruption of futile folding attempts in the ER lumen, deliver terminally misfolded polypeptides to translocons at the ER membrane, dislocate them into the cytosol, ensure poly-ubiquitylation, and proteasomal degradation (Guerriero & Brodsky, 2012; Pisoni & Molinari, 2016). Degradation of aberrant polypeptides that fail to enter the ERAD pathways is much less studied. However, we anticipate similar mechanistic complexity, which is highlighted, as one example, by the substrate-dependent sensitivity to activators of macroautophagy. Our study paves the way for a better understanding of the pathways ensuring removal of *compartmentalized* proteasome-resistant aggregates defined here as ER-to-lysosome-associated degradation (ERLAD). Since aggregate propagation is toxic to tissues and organisms and is linked to an expanding number of severe conformational diseases, these studies will be of medical relevance as they may lead to the identification of novel pharmacological targets.

Materials and Methods

Expression plasmids and antibodies

ATZ was subcloned in pcDNA3.1 expression plasmid with addition of a C-terminus HA tag or N-terminus HaloTag. FAM134B-HA and FAM134BLIR-HA (DDFELL to AAAAAA) expression plasmids were purchased from GenScript. HA tag was replaced by a V5 tag. Plasmids encoding GFP-LC3 and sfGFP-KDEL were a gift from N. Mizushima and E. Snapp, respectively. For the generation of Split GFP construct, FAM134B was tagged at the C-terminus with a linker (*italic*) of 28 amino acids followed by the eleventh β strand of GFP (T11,GCGGCCCGCGGACCCGGGAGCGCGGTGAGGGCTCAGCCGCGGAGGACCCGGTCCGGAGGCGGAAGCGGGATATCAGGTTTCAGAGAA GAGGGACCACATGCTGCTGCTGGAGTACGTGACCGCCGCGGCATCACCGACGCCTC) and the N-terminus of LC3 with the remaining portion of GFP (GFP1–10), which lacks fluorescence ability. Commercial antibodies used in this study were against polymeric ATZ (2C1, HycultBiotech), GAPDH (Merck), HA (Sigma), HA probe F7 (Santa Cruz Biotech.), LAMP1 (Hybridoma Bank, 1D4B was deposited to the DSHB by August, J.T.), LC3 (Sigma), STX17 (Sigma), VAMP8 (Abcam), V5 (Invitrogen), CLIMP63 (Proteintech),

p62 (MBL), Actin (Santa Cruz Biotech.), LC3B (Novus), GFP (Abcam), ATG4B (Sigma), ATG7 (Sigma), ATG1/ULK1 (Sigma), ATG13 (Sigma), ATG9A (Sigma), Rubicon (Abcam). Alexa-conjugated secondary antibodies were purchased from Thermo Fisher Scientific, HRP-conjugated from Jackson ImmunoResearch, and Protein A-conjugated from Invitrogen. The anti-SEC62 was a kind gift from R. Zimmermann, the anti-CNX from A. Helenius, and the anti-FAM134B from I. Kurth.

Cell culture, transient transfection, and inhibitors

Mouse embryonic fibroblasts and HEK293 cells were grown in DMEM supplemented with 10% FCS at 37°C and 5% CO₂. Transient transfections were performed using JetPrime transfection reagent (PolyPlus) following the manufacturer's protocol. BafilomycinA1 (BafA1, Calbiochem) was used at 50 nM for 12 h if not otherwise specified. Castanospermine (Sigma) used at 20 mM for 4 h as pre-treatment and then for additional 12 h together with BafA1 50 nM. SAR405 (Sigma) used at 5 μM for 5 h together with BafA1 100 nM.

CRISPR-Cas9 engineered MEF cell lines

SEC62-deficient MEF cells (CRISPR62) were engineered using CRISPR/Cas9 system as previously described (Fumagalli *et al*, 2016). FAM134B, STX17, and VAMP8 KO cells were generated as follows: for construction of the guideRNA-Cas9 plasmid, lenti-CRISPRv2-puro system (Addgene52961) was obtained from Addgene (<http://www.addgene.org>). Guide sequences were obtained from the Cas9 target design tools (crispr.mit.edu:8079 and/or www.addgene.org/pooled-library). All protocols and information can be found at the website <https://www.addgene.org/crispr>. The target sequences for guide RNA were synthesized by Microsynth. Two annealed oligonucleotides (5'-GGGTCATACTCAGCTACCT-3', 5'-AGGTAGCTGAGTATGACCC-3' for murine FAM134B, 5'-GCGCTCCAATATCCGAGAAA-3', 5'-TTTCTCGATATTGGAGCGC-3' for murine STX17, 5'-CCACCTCCGAAACAAGACAG-3', 5'-CTGTCTGTTTCGAGGTGG-3' for murine VAMP8) were inserted into the lenti-CRISPRv2-puro vector using the BsmBI restriction site. MEF cells were transfected with the plasmid JetPrime (Polyplus) according to the manufacturer's instructions to generate CRISPR134B and CRISPR17 lines. The cells were cultured in DMEM supplemented with 10% FBS. Two days after transfection, the medium was supplemented with 2 μg/ml puromycin. Puromycin-resistant clones were picked after 10 days, and gene KO was verified by WB.

Protein cross-linking with DSP

After respective treatment, HEK293 cells were washed with PBS followed by addition of 1 mM DSP (from a 100× solution in dimethylsulfoxide) in PBS. The dishes were incubated with DSP for 30 min at room temperature. The reaction was stopped by adding 1 M Tris, pH 7.8 to a final concentration of 20 mM and incubated for 15 min at room temperature. Cells were washed with PBS containing 20 mM NEM and lysed with RIPA buffer (1% Triton X-100, 0.1% SDS, 0.5% sodium deoxycholate in HBS, pH 7.4) for 20 min on ice. After a 10 min centrifugation at 10,600 g, PNS were collected and eventually used for IP. SDS-polyacrylamide gels were run under reducing conditions.

Cell lysis, immunoprecipitation, and Western blot

After the respective treatments, cells were washed with ice-cold PBS containing 20 mM NEM then lysed with 1% NP-40 (in HBS pH 7.4) or RIPA buffer (1% Triton X-100, 0.1% SDS, 0.5% sodium deoxycholate in HBS, pH 7.4) supplemented with protease inhibitors. PNS were collected after centrifugation at 10,600 g for 10 min.

Immuno-precipitations were performed diluting PNS with respective lysis buffer and incubating it with Protein G beads (VWR, 1:10 w/v, swollen in PBS) and the antibody against the protein of interest or V5-conjugated beads (Sigma), at 4°C. After three washes of the immunoprecipitates with 0.5% Triton X-100, beads were denatured for 5 min at 95°C and subjected to SDS-PAGE. Proteins were transferred to PVDF membranes using the Trans-Blot Turbo Transfer System (Bio-Rad). Membranes were blocked with 10% (w/v) non-fat dry milk (Bio-Rad) in TBS-T and stained with primary antibodies diluted in TBS-T followed by HRP-conjugated secondary antibodies or Protein A diluted in TBS-T. Membranes were developed using Luminata Forte ECL detection system (Millipore) and signals captured on an Amersham Imager 680 system or LAS4000 (GE Healthcare Life Sciences). Images were quantified with the Multi Gauge Analysis software (Fujifilm). Membrane stripping for probing additional antigens was done using Re-Blot Plus Strong Solution (Millipore) following the manufacturer's instructions.

Confocal laser scanning microscopy

Mouse embryonic fibroblasts plated on alcian blue-treated glass coverslips were DMSO or BafA1 treated for 12 h. Cells were then washed twice in PBS and fixed at room temperature for 20 min in 3.7% formaldehyde diluted in PBS. Antigen accessibility was enhanced by 15-min incubation with permeabilization solution (PS, 0.05% saponin, 10% goat serum, 10 mM HEPES, 15 mM glycine). Cells were incubated with the primary antibodies diluted 1:100 in PS for 90 min, washed for 15 min in PS, and then incubated with Alexa Fluor-conjugated secondary antibodies diluted 1:300 in PS for 45 min. Cells were rinsed with PS and water and mounted with Vectashield (Vector Laboratories) supplemented with 40,6-diamidino-2-phenylindole (DAPI). Confocal pictures were acquired on a Leica TCS SP5 microscope with a Leica HCX PL APO lambda blue 63.0 × 1.40 OIL UV objective. Figure 2H was acquired with Leica HCS PL APO CS 100 × 1.44 OIL UV objective with a XY pixel size of 37 nm and XZ pixel size of 83 nm and pinhole 0.8 AU. Image was then deconvolved with Autoquant 3.1.1 (Media Cybernetics) with spherical aberration correction. Image analysis and quantification were performed with FIJI (Schindelin *et al*, 2012) after blinded randomization. Image processing was also done with Photoshop (Adobe).

Flow cytometry

Mouse embryonic fibroblasts were plated in a 12-well plate and transfected with JetPrime reagent following the manufacturer's protocol. Seventeen hours after transfection, cells were treated with the respective drugs or mock-treated for 12 h. Cells were detached and collected, washed with PBS, fixed with 3.7% PFA in PBS for 20 min at RT, washed three times in PBS, and permeabilized with saponin solution (5% goat serum, 15 mM glycine, 0.05% saponin, 10 mM HEPES in PBS). Primary antibodies were diluted in saponin

solution and added for 1 h at RT, followed by three washes in PBS after which fluorophore-conjugated secondary antibodies diluted in saponin solution were added for 45 min at RT. Finally, cells were washed three times in PBS, resuspended in MACS buffer (PBS with 2% FCS and 2 mM EDTA), and run on a FACSCanto II flow cytometer (BD Biosciences). Data were analyzed and annotated with using FlowJo software (FlowJo LLC).

Halo pulse-chase analysis

For CLSM analysis, mouse embryonic fibroblasts cells were plated on alcian blue coverslip and transfected with HaloTag-ATZ or with HaloTag-ATZ and sfGFP-KDEL as reported above. Seventeen hours after transfection, cells were incubated for 30 min with 15 μ M 6-Chlorohexanol (Sigma) in DMEM 10% FCS, a cell-permeable black ligand that irreversibly occupied the HaloTag-binding pocket. After three washes in DMEM 10% FCS, cells were incubated for 15 min with 1 μ M PBI 5030 far red ligand (Promega) which exclusively enters the HaloTag ligand-binding pocket of newly synthesized HaloTag-ATZ. After three washes in DMEM 10% FCS, the fluorescent ligand is again replaced with 15 μ M 6-Chlorohexanol to block incorporation of the fluorescent ligand in the newly synthesized HaloTag-ATZ. For biochemical analysis shown in Fig EV5A, HEK293 cells were transfected with HaloTag-ATZ and pulsed with TMR (Promega). Cells were fixed or lysed after 30, 120, 180, and 300 min of chase and processed for CLSM or for SDS-PAGE as reported above. Time-course quantification of fluorescence co-localization between HaloTag-ATZ, sfGFP-KDEL, CNX, or CLIMP63 shown in Fig 6G was made using a custom-developed CellProfiler (Carpenter *et al*, 2006) pipeline (segmentation of the two markers, followed by the measurement of the area of colocalizing pixels). For biochemical analysis shown in Fig EV5A, after SDS-PAGE gels were scanned with the Typhoon FLA 9500 (Software Version 1.0). Bands were quantified using the ImageQuant software (Molecular Dynamics, GE Healthcare).

Immunogold electron microscopy

Cells were plated on alcian blue coverslips, transfected and fixed with 3.7% formaldehyde as reported above. After washes in PBS and 50 mM glycine, cells were permeabilized with 0.25% saponin, 0.1% BSA, and blocked in blocking buffer (0.2% BSA, 5% goat serum, 50 mM NH₄Cl, 0.1% saponin, 20 mM PO₄ buffer, 150 mM NaCl). Staining with primary antibodies and nanogold-labeled secondary antibodies (Nanoprobes) was performed in blocking buffer at room temperature. Cells were re-fixed in 1% glutaraldehyde, and nanogold was enlarged with gold enhancement solution (Nanoprobes) according to the manufacturer's instructions. Cells were post-fixed with osmium tetroxide, embedded in epon, and processed into ultrathin slices. After contrasting with uranyl acetate and lead citrate, sections were analyzed with a Zeiss LEO 512 electron microscope. Images were acquired by a 2k bottom-mounted slow-scan Proscan camera controlled by EsvisionPro 3.2 software. Image analysis and quantification were performed with FIJI.

Electron tomography

For electron tomography, 200- to 250-nm-thick sections were collected on formvar-coated copper slot grids, and gold fiducials

(10 nm) were applied on both surfaces of the grids. The samples were imaged in a 200 kV Tecnai G2 20 electron microscope (FEI, Eindhoven, The Netherlands) at magnification of 9.6k resulting in a pixel size of 2.29 nm. Tilted images (+60/−60 according to a Saxton scheme) were acquired using Xplorer 3D (FEI) with an Eagle 2k × 2k CCD camera (FEI). Tilted series alignment and tomography reconstruction were done with the IMOD software package (Mastrorade, 1997). Segmentation and 3D visualization were done with Microscopy Image Browser (Belevich *et al*, 2016) and IMOD software packages.

Correlative light-electron microscopy (CLEM)

Cells were grown on finder grids and prepared for IEM as described above. Z-stacks of cells of interest were taken with the PerkinElmer UltraView ERS confocal microscope. The coordinates of the cells on the finder grid were determined by bright-field microscopy. Cells were fixed in 1% glutaraldehyde in 0.1 M cacodylate buffer (Sigma) and post-fixed with 1.5% potassium ferricyanide, 1% OsO₄ in 0.1 M cacodylate buffer. Cells were stained with 0.5% uranyl acetate overnight, dehydrated in ethanol, and embedded in epon. After baking for 48 h at 60°C, the resin was released from the glass coverslip by temperature shock in liquid nitrogen. Serial sections (70–90 nm) were collected on carbon-coated formvar slot grids and imaged with a Zeiss LEO 512 electron microscope. Images were acquired by a 2k × 2k bottom-mounted slow-scan Proscan camera controlled by EsvisionPro 3.2 software. Immunofluorescence and IEM images were aligned using Icy bioimage analysis.

Amino acid starvation

To induce autophagy, cells were washed three times with Earle's balanced salt solution (EBSS, Thermo Fisher) and then incubated in EBSS as indicated.

Statistical analysis

Plots and statistical analyses were performed using GraphPad Prism 7 (GraphPad Software Inc.). In this study, one-way ANOVA with Dunnett's multiple comparisons test and unpaired two-tailed *t*-test were used to assess statistical significance. An adjusted *P*-value < 0.05 (for one-way ANOVA with Dunnett's multiple comparisons test) or *P*-value < 0.05 (for *t*-test) was considered as statistically significant.

Expanded View for this article is available online.

Acknowledgements

We thank G. Hämmerling, J.-L. Guan, D. Green, J. Gruenberg, A. Helenius, M. Komatsu, I. Kurth, G. Marino, M. Michalak, N. Mizushima, F. Reggiori, T. Saitoh, C. Settembre, E. Snapp, S. Toozee, R. Zimmermann, G. Van der Goot, X. Wang, and the members of Molinari's laboratory for gift of reagents, discussions, and critical reading of the manuscript. We are grateful to the ALEMbic facility at San Raffaele Scientific Institute, Milan, Italy, for the help in electron microscopy analysis. M.M. is supported by Signora Alessandra, AlphaONE Foundation, Foundation for Research on Neurodegenerative Diseases, the Novartis Foundation, Swiss National Science Foundation (SNF), and Comel and Gelu Foundations. P.P. is supported by SNF.

Author contributions

Conceptualization: MM, IF, EF, and EvA; Methodology: IF, EF, AR, RD'A, DM, AD, PP, EvA, and MM; Investigation: IF, EF, TJB, ML, TS, CG, and MM; Writing—original draft: MM; Writing—review & editing: IF, EF, ML, PP, EvA, and MM; Supervision: MM.

Conflict of interest

The authors declare that they have no conflict of interest.

References

- Belevich I, Joensuu M, Kumar D, Vihinen H, Jokitalo E (2016) Microscopy image browser: a platform for segmentation and analysis of multidimensional datasets. *PLoS Biol* 14: e1002340
- Bento CF, Renna M, Ghislat G, Puri C, Ashkenazi A, Vicinanza M, Menzies FM, Rubinsztein DC (2016) Mammalian autophagy: how does it work? *Annu Rev Biochem* 85: 685–713
- Bestebroer J, V'Kovski P, Mauthe M, Reggiori F (2013) Hidden behind autophagy: the unconventional roles of ATG proteins. *Traffic* 14: 1029–1041
- Cabantous S, Terwilliger TC, Waldo GS (2005) Protein tagging and detection with engineered self-assembling fragments of green fluorescent protein. *Nat Biotechnol* 23: 102–107
- Caramelo JJ, Parodi AJ (2007) How sugars convey information on protein conformation in the endoplasmic reticulum. *Semin Cell Dev Biol* 18: 732–742
- Carpenter AE, Jones TR, Lamprecht MR, Clarke C, Kang IH, Friman O, Guertin DA, Chang JH, Lindquist RA, Moffat J, Golland P, Sabatini DM (2006) Cell Profiler: image analysis software for identifying and quantifying cell phenotypes. *Genome Biol* 7: R100
- Chu AS, Perlmutter DH, Wang Y (2014) Capitalizing on the autophagic response for treatment of liver disease caused by alpha-1-antitrypsin deficiency and other genetic diseases. *Biomed Res Int* 2014: 459823
- Cieri D, Vicario M, Giacomello M, Vallese F, Filadi R, Wagner T, Pozzan T, Pizzo P, Scorrano L, Brini M, Cali T (2018) SPLICS: a split green fluorescent protein-based contact site sensor for narrow and wide heterotypic organelle juxtaposition. *Cell Death Differ* 25: 1131–1145
- Denzel A, Molinari M, Trigueros C, Martin JE, Velmurgan S, Brown S, Stamp G, Owen MJ (2002) Early postnatal death and motor disorders in mice congenitally deficient in calnexin expression. *Mol Cell Biol* 22: 7398–7404
- Dickens JA, Ordonez A, Chambers JE, Beckett AJ, Patel V, Malzer E, Dominicus CS, Bradley J, Peden AA, Prior IA, Lomas DA, Marciniak SJ (2016) The endoplasmic reticulum remains functionally connected by vesicular transport after its fragmentation in cells expressing Z-alpha(1)-antitrypsin. *FASEB J* 30: 4083–4097
- Elbein AD (1991) Glycosidase inhibitors: inhibitors of N-linked oligosaccharide processing. *FASEB J* 5: 3055–3063
- England CG, Luo HM, Cai WB (2015) HaloTag technology: a versatile platform for biomedical applications. *Bioconjug Chem* 26: 975–986
- Fregno I, Molinari M (2018) Endoplasmic reticulum turnover: ER-phagy and other flavors in selective and non-selective ER clearance. *F1000Res* 7: 454
- Fujita E, Kouroku Y, Isoai A, Kumagai H, Misutani A, Matsuda C, Hayashi YK, Momoi T (2007) Two endoplasmic reticulum-associated degradation (ERAD) systems for the novel variant of the mutant dysferlin: ubiquitin/proteasome ERAD(I) and autophagy/lysosome ERAD(II). *Hum Mol Genet* 16: 618–629
- Fumagalli F, Noack J, Bergmann TJ, Presmanes EC, Pisoni GB, Fasana E, Fregno I, Galli C, Loi M, Soldà T, D'Antuono R, Raimondi A, Jung M, Melnyk A, Schorr S, Schreiber A, Simonelli L, Varani L, Wilson-Zbinden C, Zerbe O et al (2016) Translocon component Sec62 acts in endoplasmic reticulum turnover during stress recovery. *Nat Cell Biol* 18: 1173–1184
- Gelling CL, Dawes IW, Perlmutter DH, Fisher EA, Brodsky JL (2012) The endosomal protein-sorting receptor sortilin has a role in trafficking alpha-1 antitrypsin. *Genetics* 192: 889–903
- Grumati P, Morozzi G, Holper S, Mari M, Harwardt MI, Yan R, Muller S, Reggiori F, Heilemann M, Dikic I (2017) Full length RTN3 regulates turnover of tubular endoplasmic reticulum via selective autophagy. *eLife* 6: e25555
- Guerriero CJ, Brodsky JL (2012) The delicate balance between secreted protein folding and endoplasmic reticulum-associated degradation in human physiology. *Physiol Rev* 92: 537–576
- Hara T, Takamura A, Kishi C, Iemura SI, Natsume T, Guan JL, Mizushima N (2008) FIP200, a ULK-interacting protein, is required for autophagosome formation in mammalian cells. *J Cell Biol* 181: 497–510
- Hebert DN, Foellmer B, Helenius A (1995) Glucose trimming and reglucosylation determine glycoprotein association with calnexin in the endoplasmic reticulum. *Cell* 81: 425–433
- Hidvegi T, Ewing M, Hale P, Dippold C, Beckett C, Kemp C, Maurice N, Mukherjee A, Goldbach C, Watkins S, Michalopoulos G, Perlmutter DH (2010) An autophagy-enhancing drug promotes degradation of mutant alpha 1-antitrypsin Z and reduces hepatic fibrosis. *Science* 329: 229–232
- Hosokawa N, Hara T, Kaizuka T, Kishi C, Takamura A, Miura Y, Iemura S, Natsume T, Takehana K, Yamada N, Guan JL, Oshiro N, Mizushima N (2009) Nutrient-dependent mTORC1 association with the ULK1-Atg13-FIP200 complex required for autophagy. *Mol Biol Cell* 20: 1981–1991
- Houck SA, Ren HY, Madden VJ, Bonner JN, Conlin MP, Janovick JA, Conn PM, Cyr DM (2014) Quality control autophagy degrades soluble ERAD-resistant conformers of the misfolded membrane protein GnrHR. *Mol Cell* 54: 166–179
- Huotari J, Helenius A (2011) Endosome maturation. *EMBO J* 30: 3481–3500
- Hurley JH, Young LN (2017) Mechanisms of autophagy initiation. *Annu Rev Biochem* 86: 225–244
- Ishida Y, Yamamoto A, Kitamura A, Lamande SR, Yoshimori T, Bateman JF, Kubota H, Nagata K (2009) Autophagic elimination of misfolded procollagen aggregates in the endoplasmic reticulum as a means of cell protection. *Mol Biol Cell* 20: 2744–2754
- Kaizuka T, Mizushima N (2016) Atg13 is essential for autophagy and cardiac development in mice. *Mol Cell Biol* 36: 585–595
- Kakuta S, Yamaguchi J, Suzuki C, Sasaki M, Kazuno S, Uchiyama Y (2017) Small GTPase Rab1B is associated with ATG9A vesicles and regulates autophagosome formation. *FASEB J* 31: 3757–3773
- Kamimoto T, Shoji S, Hidvegi T, Mizushima N, Umebayashi K, Perlmutter DH, Yoshimori T (2006) Intracellular inclusions containing mutant alpha1-antitrypsin Z are propagated in the absence of autophagic activity. *J Biol Chem* 281: 4467–4476
- Khaminets A, Heinrich T, Mari M, Grumati P, Huebner AK, Akutsu M, Liebmann L, Stolz A, Nietzsche S, Koch N, Mauthe M, Katona I, Qualmann B, Weis J, Reggiori F, Kurth I, Hubner CA, Dikic I (2015) Regulation of endoplasmic reticulum turnover by selective autophagy. *Nature* 522: 354–358
- Klionsky DJ, Elazar Z, Seglen PO, Rubinsztein DC (2008) Does bafilomycin A(1) block the fusion of autophagosomes with lysosomes? *Autophagy* 4: 849–850

- Komatsu M, Waguri S, Ueno T, Iwata J, Murata S, Tanida I, Ezaki J, Mizushima N, Ohsumi Y, Uchiyama Y, Kominami E, Tanaka K, Chiba T (2005) Impairment of starvation-induced and constitutive autophagy in Atg7-deficient mice. *J Cell Biol* 169: 425–434
- Kroeger H, Miranda E, MacLeod I, Perez J, Crowther DC, Marciniak SJ, Lomas DA (2009) Endoplasmic reticulum-associated degradation (ERAD) and autophagy cooperate to degrade polymerogenic mutant serpins. *J Biol Chem* 284: 22793–22802
- Ktistakis NT, Tooze SA (2016) Digesting the expanding mechanisms of autophagy. *Trends Cell Biol* 26: 624–635
- Lamark T, Johansen T (2012) Aggrephagy: selective disposal of protein aggregates by macroautophagy. *Int J Cell Biol* 2012: 1–21
- Liu Y, Choudhury P, Cabral CM, Sifers RN (1999) Oligosaccharide modification in the early secretory pathway directs the selection of a misfolded glycoprotein for degradation by the proteasome. *J Biol Chem* 274: 5861–5867
- Loi M, Fregno I, Guerra C, Molinari M (2018) Eat it right: ER-Phagy and RecovER-Phagy. *Biochem Soc Trans* 46: 699–706
- Marciniak SJ, Ordonez A, Dickens JA, Chambers JE, Patel V, Dominicus CS, Malzer E (2016) New concepts in alpha-1 antitrypsin deficiency disease mechanisms. *Ann Am Thorac Soc* 13(Suppl 4): 289–296
- Marino G, Fernandez AF, Cabrera S, Lundberg YW, Cabanillas R, Rodriguez F, Salvador-Montoliu N, Vega JA, Germana A, Fueyo A, Freije JMP, Lopez-Otin C (2010) Autophagy is essential for mouse sense of balance. *J Clin Invest* 120: 2331–2344
- Martinez J, Malireddi RKS, Lu Q, Cunha LD, Pelletier S, Gingras S, Orchard R, Guan JL, Tan HY, Peng JM, Kanneganti TD, Virgin HW, Green DR (2015) Molecular characterization of LC3-associated phagocytosis reveals distinct roles for Rubicon, NOX2 and autophagy proteins. *Nat Cell Biol* 17: 893–906
- Mastrorarde DN (1997) Dual-axis tomography: an approach with alignment methods that preserve resolution. *J Struct Biol* 120: 343–352
- McAlpine F, Williamson LE, Tooze SA, Chan EYW (2013) Regulation of nutrient-sensitive autophagy by uncoordinated 51-like kinases 1 and 2. *Autophagy* 9: 361–373
- Menzies FM, Fleming A, Caricasole A, Bento CF, Andrews SP, Ashkenazi A, Fullgrabe J, Jackson A, Sanchez MJ, Karabiyik C, Licitra F, Ramirez AL, Pavel M, Puri C, Renna M, Ricketts T, Schlotawa L, Vicinanza M, Won H, Zhu Y et al (2017) Autophagy and neurodegeneration: pathogenic mechanisms and therapeutic opportunities. *Neuron* 93: 1015–1034
- Miranda E, Perez J, Ekeowa UI, Hadzic N, Kalsheker N, Gooptu B, Portmann B, Belorgey D, Hill M, Chambers S, Teckman J, Alexander GJ, Marciniak SJ, Lomas DA (2010) A novel monoclonal antibody to characterize pathogenic polymers in liver disease associated with alpha(1)-antitrypsin deficiency. *Hepatology* 52: 1078–1088
- Mizushima N, Yoshimori T, Ohsumi Y (2011) The role of Atg proteins in autophagosome formation. *Annu Rev Cell Dev Biol* 27: 107–132
- Molinari M, Calanca V, Galli C, Lucca P, Paganetti P (2003) Role of EDEM in the release of misfolded glycoproteins from the calnexin cycle. *Science* 299: 1397–1400
- Molinari M, Eriksson KK, Calanca V, Galli C, Cresswell P, Michalak M, Helenius A (2004) Contrasting functions of calreticulin and calnexin in glycoprotein folding and ER quality control. *Mol Cell* 13: 125–135
- Molinari M, Galli C, Vanoni O, Arnold SM, Kaufman RJ (2005) Persistent glycoprotein misfolding activates the glucosylase II/UGT1-driven calnexin cycle to delay aggregation and loss of folding competence. *Mol Cell* 20: 503–512
- Noda T, Faruqhar MG (1992) A non-autophagic pathway for diversion of ER secretory proteins to lysosomes. *J Cell Biol* 119: 85–97
- Oda Y, Hosokawa N, Wada I, Nagata K (2003) EDEM as an acceptor of terminally misfolded glycoproteins released from calnexin. *Science* 299: 1394–1397
- Olivari S, Molinari M (2007) Glycoprotein folding and the role of EDEM1, EDEM2 and EDEM3 in degradation of folding-defective glycoproteins. *FEBS Lett* 581: 3658–3664
- Pastore N, Blomenkamp K, Annunziata F, Piccolo P, Mithbaakar P, Maria Sepe R, Vetrini F, Palmer D, Ng P, Polishchuk E, Iacobacci S, Polishchuk R, Teckman J, Ballabio A, Brunetti-Pierri N (2013) Gene transfer of master autophagy regulator TFEB results in clearance of toxic protein and correction of hepatic disease in alpha-1-anti-trypsin deficiency. *EMBO Mol Med* 5: 397–412
- Pieren M, Galli C, Denzel A, Molinari M (2005) The use of calnexin and calreticulin by cellular and viral glycoproteins. *J Biol Chem* 280: 28265–28271
- Pisoni GB, Molinari M (2016) Five questions (with their Answers) on ER-associated degradation. *Traffic* 17: 341–350
- Ronan B, Flamand O, Vescovi L, Dureuil C, Durand L, Fassy F, Bachelot MF, Lambertson A, Mathieu M, Bertrand T, Marquette JP, El-Ahmad Y, Filoche-Romme B, Schio L, Garcia-Echeverria C, Goulaouic H, Pasquier B (2014) A highly potent and selective Vps34 inhibitor alters vesicle trafficking and autophagy. *Nat Chem Biol* 10: 1013–1019
- Saitoh T, Fujita N, Hayashi T, Takahara K, Satoh T, Lee H, Matsunaga K, Kageyama S, Omori H, Noda T, Yamamoto N, Kawai T, Ishii K, Takeuchi O, Yoshimori T, Akira S (2009) Atg9a controls dsDNA-driven dynamic translocation of STING and the innate immune response. *Proc Natl Acad Sci USA* 106: 20842–20846
- Sardiello M, Palmieri M, di Ronza A, Medina DL, Valenza M, Gennarino VA, Di Malta C, Donaudo F, Embrione V, Polishchuk RS, Banfi S, Parenti G, Cattaneo E, Ballabio A (2009) A gene network regulating lysosomal biogenesis and function. *Science* 325: 473–477
- Schindelin J, Arganda-Carreras I, Frise E, Kaynig V, Longair M, Pietzsch T, Preibisch S, Rueden C, Saalfeld S, Schmid B, Tinevez JY, White DJ, Hartenstein V, Eliceiri K, Tomancak P, Cardona A (2012) Fiji: an open-source platform for biological-image analysis. *Nat Methods* 9: 676–682
- Schubert U, Anton LC, Gibbs J, Norbury CC, Yewdell JW, Bennink JR (2000) Rapid degradation of a large fraction of newly synthesized proteins by proteasomes. *Nature* 404: 770–774
- Shang L, Chen S, Du F, Li S, Zhao L, Wang X (2011) Nutrient starvation elicits an acute autophagic response mediated by Ulk1 dephosphorylation and its subsequent dissociation from AMPK. *Proc Natl Acad Sci USA* 108: 4788–4793
- Smith MD, Harley ME, Kemp AJ, Wills J, Lee M, Arends M, von Kriegsheim A, Behrends C, Wilkinson S (2018) CCPG1 is a non-canonical autophagy cargo receptor essential for ER-phagy and pancreatic ER proteostasis. *Dev Cell* 44: 217–232
- Soldà T, Garbi N, Hammerling GJ, Molinari M (2006) Consequences of ERp57 deletion on oxidative folding of obligate and facultative clients of the calnexin cycle. *J Biol Chem* 281: 6219–6226
- Soldà T, Galli C, Kaufman RJ, Molinari M (2007) Substrate-specific requirements for UGT1-dependent release from calnexin. *Mol Cell* 27: 238–249
- Steehmaier M, Oorschot V, Klumperman J, Scheller RH (2000) Syntaxin 17 is abundant in steroidogenic cells and implicated in smooth endoplasmic reticulum membrane dynamics. *Mol Biol Cell* 11: 2719–2731

- Suzuki K, Kubota Y, Sekito T, Ohsumi Y (2007) Hierarchy of Atg proteins in pre-autophagosomal structure organization. *Genes Cells* 12: 209–218
- Teckman JH, Perlmutter DH (2000) Retention of mutant alpha(1)-antitrypsin Z in endoplasmic reticulum is associated with an autophagic response. *Am J Physiol Gastrointest Liver Physiol* 279: G961–G974
- Teckman JH, An JK, Loethen S, Perlmutter DH (2002) Fasting in alpha1-antitrypsin deficient liver: constitutive activation of autophagy. *Am J Physiol Gastrointest Liver Physiol* 283: G1156–G1165
- Uhlen M, Fagerberg L, Hallstrom BM, Lindskog C, Oksvold P, Mardinoglu A, Sivertsson A, Kampf C, Sjostedt E, Asplund A, Olsson I, Edlund K, Lundberg E, Navani S, Szigartyo CA, Odeberg J, Djureinovic D, Takanen JO, Hober S, Alm T et al (2015) Tissue-based map of the human proteome. *Science* 347: 1260419
- Vabulas RM, Hartl FU (2005) Protein synthesis upon acute nutrient restriction relies on proteasome function. *Science* 310: 1960–1963